LA-UR-95-4456

Los Alamos National Laboratory is operated by the University of California for the United States Department of Energy under contract W-7405-ENG-36.

TITLE:

Plume Dispersion Sensitivity To Upper-level Wind Variations In A Chilean Coastal Environment

AUTHOR(S): Michael J. Brown, TSA-4
Michael D. Williams, TSA-4

SUBMITTED TO: Air & Waste Management Association 89th Annual Meeting and Exhibition
June 1996

Los Alamos

Los Alamos National Laboratory
Los Alamos, New Mexico 87545

FORM NO. 836 R4
ST. NO. 2629 5/81

Plume Dispersion Sensitivity To Upper-level Wind Variations In A Chilean Coastal Environment

Michael J. Brown and Michael D. Williams

Los Alamos National Laboratory
Energy and Environmental Assessment
Group TSA-4, MS F604
Los Alamos, NM 87545
e-mail: brown@viento.lanl.gov

INTRODUCTION

Government and industry leaders in Chile are concerned with the impact of coastal smelter emissions on the air quality of surrounding communities and the inland capitol city of Santiago. The smelter emissions contain large amounts of sulfur and heavy metals.[1] Because several large smelters are located along the coast, an air quality modeling system must be able to handle flow in both a coastal and mountainous environment. Linked seabreeze and mountain-induced slope flows which change in time and space have been best handled using prognostic numerical models.[2,3,4] We are using a prognostic mesoscale meteorological model (HOTMAC - Higher-Order Turbulence Model for Atmospheric Circulation) linked to a random walk/puff model (RAPTAD - RAndom Particle Transport and Dispersion) in order to simulate plume transport over hundreds of kilometers. In this paper, we present plume dispersion simulations resulting from 90˚ incremental changes in the prescribed wind direction. These tests were motivated by our desire to develop a climatology of plume transport direction based on prevailing wind direction, as well as to evaluate the effect of the uncertainties inherent in rawinsonde wind measurements and large-scale weather wind-field forecasts, which are often used as input to meteorological models.

MODEL DESCRIPTION

HOTMAC. HOTMAC is a three-dimensional time-dependent mesoscale meteorological model utilizing a 1 $^1/_2$ order turbulence closure scheme[5]. Using the hydrostatic approximation, a gradient-diffusion closure scheme for the horizontal turbulence components, and a terrain-following coordinate system, the governing conservation equations for mass, momentum, heat, and moisture are

$$\frac{\partial \bar{U}}{\partial x} + \frac{\partial \bar{V}}{\partial y} + \frac{\partial \overline{W^*}}{\partial z^*} - \frac{1}{H - z_g}\left(\bar{U}\frac{\partial z_g}{\partial x} + \bar{V}\frac{\partial z_g}{\partial y}\right) = 0 \tag{1}$$

$$\frac{D\bar{U}}{Dt} = f(\bar{V} - \bar{V}_g) + g\frac{\bar{H} - z^*}{\bar{H}}\left(1 - \frac{\langle\bar{\Theta}_v\rangle}{\bar{\Theta}_v}\right)\frac{\partial z_g}{\partial x} + \frac{\partial}{\partial x}\left(K_x\frac{\partial \bar{U}}{\partial x}\right) + \frac{\partial}{\partial y}\left(K_{xy}\frac{\partial \bar{U}}{\partial y}\right) + \frac{\bar{H}}{H - z_g}\frac{\partial}{\partial z^*}(-\overline{uw}) \tag{2}$$

$$\frac{D\bar{V}}{Dt} = -f(\bar{U} - \bar{U}_g) + g\frac{\bar{H} - z^*}{\bar{H}}\left(1 - \frac{\langle\bar{\Theta}_v\rangle}{\bar{\Theta}_v}\right)\frac{\partial z_g}{\partial y} + \frac{\partial}{\partial x}\left(K_{xy}\frac{\partial \bar{V}}{\partial x}\right) + \frac{\partial}{\partial y}\left(K_y\frac{\partial \bar{V}}{\partial y}\right) + \frac{\bar{H}}{H - z_g}\frac{\partial}{\partial z^*}(-\overline{vw}) \tag{3}$$

$$\frac{D\bar{\Theta}_v}{Dt} = \frac{\partial}{\partial x}\left[K_x\frac{\partial \bar{\Theta}_v}{\partial x}\right] + \frac{\partial}{\partial y}\left[K_y\frac{\partial \bar{\Theta}_v}{\partial y}\right] + \frac{\bar{H}}{H - z_g}\left[\frac{\partial}{\partial z^*}(-\overline{w\theta_v}) + \frac{1}{\rho C_p}\frac{\partial R_N}{\partial z^*}\right] \tag{4}$$

$$\frac{D\bar{Q}_v}{Dt} = \frac{\partial}{\partial x}\left[K_x\frac{\partial \bar{Q}_v}{\partial x}\right] + \frac{\partial}{\partial y}\left[K_y\frac{\partial \bar{Q}_v}{\partial y}\right] + \frac{\bar{H}}{H - z_g}\frac{\partial}{\partial z^*}(-\overline{wq_v}) \tag{5}$$

where the overbar denotes an ensemble average, U, V, Θ_v, and Q_v are the x (east-west) and y (north-south) wind components, the virtual potential temperature, and the moisture content, respectively. U_g and V_g are the x and y geostrophic wind components, *f* is the Coriolis parameter, g is gravity, ρ is density, C_p is specific heat, and R_N is the net radiation. W_* and z_* are the transformed vertical velocity and height, respectively,

$$\overline{W^*} = \frac{\bar{H}}{H - z_g}\overline{W} + \frac{z^* - \bar{H}}{H - z_g}\left(\bar{U}\frac{\partial z_g}{\partial x} + \bar{V}\frac{\partial z_g}{\partial y}\right) \tag{6}$$

$$z^* = \bar{H}\frac{z - z_g}{H - z_g} \tag{7}$$

where H is the maximum domain depth in real space, $\bar{H}$ is the domain depth in the terrain-following coordinate system, and z_g is the ground elevation. The momentum, heat, and moisture fluxes are approximated using a one-equation $1\,{}^1/_2$ order turbulence closure scheme[6,7]

$$[\overline{uw},\overline{vw}] = -l q \tilde{S}_M\left[\frac{\partial \bar{U}}{\partial z}, \frac{\partial \bar{V}}{\partial z}\right] \tag{8}$$

$$[\overline{w\theta_v},\overline{wq_v}] = -\alpha l q \tilde{S}_M\left[\frac{\partial \bar{\Theta}_v}{\partial z}, \frac{\partial \bar{Q}_v}{\partial z}\right] \tag{9}$$

where the turbulent length scale *l* is determined from an algebraic equation, $\tilde{S}_M$ and α are functions of the flux Richardson number, and the turbulent kinetic energy q^2 is solved by the approximate equation

$$\frac{D}{Dt}\left(\frac{q^2}{2}\right) = \frac{\partial}{\partial x}\left[K_x\frac{\partial}{\partial x}\left(\frac{q^2}{2}\right)\right] + \frac{\partial}{\partial y}\left[K_y\frac{\partial}{\partial y}\left(\frac{q^2}{2}\right)\right] + \left(\frac{\bar{H}}{H - z_g}\right)^2\frac{\partial}{\partial z^*}\left[q l S_q\frac{\partial}{\partial z^*}\left(\frac{q^2}{2}\right)\right] - \frac{\bar{H}}{H - z_g}\left(\overline{uw}\frac{\partial \bar{U}}{\partial z^*} + \overline{vw}\frac{\partial \bar{V}}{\partial z^*}\right) \tag{10}$$

The equations are solved numerically using the alternating direction implicit (ADI) finite difference scheme. A simple 4-point diffusive smoothing scheme with smoothing parameter $\gamma = 0.3$ is used to remove $2\,\Delta x$ waves. A nudging scheme[8] and a local-wind correction scheme[9] have been used in these simulations. HOTMAC also includes solar and terrestrial radiation effects, as well as drag and radiation effects of forest canopies. The lower boundary conditions are defined by a surface energy balance and similarity theory. The soil heat flux is obtained by solving a 5-level heat conduction equation in the soil which ignores lateral heat transfer.

RAPTAD. RAPTAD is a Monte-Carlo dispersion and transport code combining the attributes of random-walk and puff dispersion models.[10] Pseudo-particles are transported with instantaneous velocities that include the mean wind field and the turbulent velocities. The turbulent velocity is generated using the Monte-Carlo random-walk equation

$$u_i(t + \Delta t) = \exp(-\Delta t/T_L)\cdot u_i(t) + \{1 - \exp(2\Delta t/T_L)\}\cdot\sigma_u\cdot\varsigma, \tag{11}$$

where T_L is the Lagrangian timescale, σ_u is the standard deviation of the velocity fluctuations, and ς is a

random variable chosen from a Gaussian distribution and standard deviation equal to one. The location of each pseudo-particle represents the center of mass of a concentration distribution for each puff. The total concentration at any point is obtained by adding the concentration contributions of each puff at that point (a kernel method). Each puff is assumed to have a Gaussian distribution where variances are determined from the time integration of the velocity variances encountered over the history of the puff. The variances are estimated based on the random force theory of turbulent diffusion.[11] Plume-rise is computed using the Briggs formulae.[12]

Modeling System Advantages. The HOTMAC-RAPTAD modeling system has many advantages for air pollution applications involving complex terrain over a multi-day period. The ADI finite difference scheme allows for a relatively large time step, thus reducing computational expense. The short and long-wave radiation schemes combined with soil heat equations allow for the simulation of time- and stratification-dependent wind, temperature, and moisture fields. The use of a higher-order turbulence model permits for the computation of horizontally-inhomogeneous turbulence fields, typical in complex terrain. The meteorological fields computed by HOTMAC are used to drive the RAPTAD transport and diffusion model. In contrast to normal Gaussian puff models, RAPTAD works well in situations where the wind directions change with height and time, e.g., in coastal and complex terrain environments. The combination random-walk/puff approach allows for faster computational speed, as fewer particles need to be released since they grow with time.

PROBLEM SET-UP

Domain. We have modeled the plume dispersion from the Ventanas copper smelter located on the Pacific coast approximately 100 km to the northwest of Santiago (see map, fig. 1). The simulations were performed on a double-nested mesh surrounding the Ventanas smelter. The location, number of grids, and grid resolution for the three mesh types are given in Table 1. An expanding vertical mesh composed of fifteen grids extending from $z^* = 0$ to 4000 m was used (see Table 2). In order to account for the mesoscale features of the flow, the model domain stretches from the Pacific Ocean in the west past the coastal range to the east and out to the crest of the Andes mountains in the east. The fine mesh allows for smaller-scale features to be resolved in the vicinity of the Ventanas smelter. The fine mesh elevation data was obtained from topographical maps, while a US Army database with elevation contours at 1000 foot intervals was used to provide topography for the larger scale meshes. Only vegetation/scrubland and water land-class properties were used in the simulation.

Meteorological Conditions. Model simulations were run with five different prevailing wind directions in 45˚ increments from 180 to 360 degrees. However, we present only the 180, 270, and 360˚ cases here in order to see clear differentiation in the model results. The upper boundary condition for the wind speed was set to 1.6 m/s, a value that represents typical summertime conditions. The winds were nudged towards hypothetical “rawinsonde measurements” made at Quinteros, a city relatively close to the Ventanas site. The “rawinsonde” wind speed profile was divided into three sections: 1) below 500 m, wind speed equals 0.1 m/s; 2) from 500 to 2000 m, wind speed linearly increases with height to 0.9 m/s; and 3) from 2000 to 4000 m, wind speed linearly increases to 1.6 m/s.

In order to remove the local-scale influences from the rawinsonde wind measurements, the model was first run with very light winds near the surface and typical upper-level winds. These model-produced wind fields were then subtracted from the rawinsonde low-level wind measurements (average wind in lowest 500 meters) in order to obtain an approximation for the large-scale driving winds. This local-wind correction scheme[9] allows for the model winds to be nudged towards the large-scale driving winds, thus accounting for the synoptic-scale forcing.

Other boundary and initial conditions were estimated using typical summertime values: the ocean temperature and the initial land temperature were set to 15 °C ; the potential temperature lapse rate was specified as +.0075 °C /m below 1000 m, +.003 °C /m from 1000 to 1500 m, +.006 °C /m from 1500 to 3000 m, and +.002 °C /m above; and the relative humidity was assigned a value of 0.70 at the surface and decreased to 0.10 at the top of the domain. The input parameters were assumed to be invariant in the horizontal direction. All simulations were started on Dec. 11 (Julian day 346) at 8:00 am local standard time (lst) and ended on Dec. 13 at 10 pm.

Stack Parameters. The Ventanas stack parameters are described in Table 3. For the purpose of simulation, we have combined the two elevated stacks at Ventanas into one combined source by assuming that the mass and volume flow rates and the buoyancy flux were additive quantities. Plume rise ranged from 150 m at night to 400 m during the day. We have not included the fugitive emissions in the present simulation. The vertical and horizontal Lagrangian timescales were set to 20 and 10,000 s, respectively.

RESULTS

HOTMAC and RAPTAD Sensitivity Tests. As mentioned earlier, we are interested in determining the impact of prevailing wind direction on plume transport. Furthermore, these tests will help us evaluate the importance of the uncertainties inherent in rawinsonde wind measurements. We now present results from the meteorological and dispersion simulations.

Meteorological Simulations. Horizontal wind vector fields computed at a ten meter height on the intermediate grid are presented in figs. 2 - 4. The inner nested grid is shown as a light gray rectangle. The Ventanas and Quinteros sites are denoted by the letters X and Q, respectively. Santiago is located just outside the southeast corner of the intermediate grid. The terrain contours are at 300 m intervals.

Figure 2 illustrates the typical night time flow pattern at a ten meter height for a prevailing wind direction of 270 degrees. The winds are small. Nocturnal drainage flow, however, has not developed. The radiative cooling of the land surface apparently is not strong enough to overcome the strong daytime upslope flow. The reasons for this unexpected result need to be further investigated. Only one vector field is shown in this figure, since differences cannot be discerned when using different prevailing wind directions.

Figure 3 depicts the 2 pm wind fields produced using a prevailing wind direction of 180 and 360 degrees. In both cases, the winds are predominately directed up the mountain slopes, a result of the rising buoyant motion induced by the warmer land surface. When comparing the two cases, few differences can be discerned in the magnitudes and directions of the wind vectors. As an aside, the relatively low wind speeds found over the ocean are a concern, as it is expected that wind speeds might be higher there due to lower surface drag. It may be that the local wind correction scheme combined with the crude averaging of the measured winds in the 0-500 m layer are responsible for the low values.

In order to see more detail, we plot wind speed and wind direction versus time ten meters above the surface at the Ventanas site in fig. 4a. The upper graph reveals that the near-surface wind speeds are similar for different prevailing wind directions. The lower graph, however, shows that the wind directions can vary up to thirty degrees. The largest differences occur, however, when the wind speeds are small.

Figure 4b depicts wind speeds and wind directions 429 meters above the Ventanas site. Here, we can see that wind speeds and wind directions are vastly different for the three prevailing wind direction cases of 180, 270, and 360 degrees. This result is of extreme importance to pollution transport, as plume rise during the daytime will result in air pollution being lifted to this height. In the lower graph, we see that the

largest difference in wind directions occur at night and that values are nearly equal to the prevailing wind direction. This result stems from the fact that the boundary-layer height is small at night (several hundred meters), thus disconnecting the flow aloft from surface processes. Daytime wind directions converge towards a value between 100 to 120 degrees. Recalling that the daytime wind direction near the ground is about 290 degrees (fig. 4a), we see evidence of a sea-breeze circulation. Wind speeds are smallest when the prevailing wind direction is 270 degrees because this is in the opposite direction of the upper-level sea-breeze winds.

Figure 5 illustrates the afternoon sea-breeze phenomenon. We have plotted the vector fields at heights of 10 and 428 m that result for a prevailing wind direction of 270 degrees. At 10 meters, strong onshore flow exists on the western half of the intermediate domain. At 428 meters, however, the winds west of 281 km utm are weak and offshore. Since the Ventanas site is near the coast, air pollution transport can be either to the west or to the east depending on the stack height, the magnitude of plume rise, and the amount of vertical mixing. In the next section, we will see how plumes from the Ventanas smelter are affected by the changing meteorological conditions.

Dispersion simulations. Simulations of plume transport and dispersion using the RAPTAD model have been accomplished by incorporating meteorological input parameters (wind, turbulence, and temperature fields) obtained from the HOTMAC simulations described in the previous section. Dispersion simulations were begun thirteen hours after the meteorological simulations were started (9:00 pm lst on Dec. 11) in order to remove HOTMAC "spin-up" effects. Figures 6 through 10 show snapshots of particle positions at different times during a forty-eight hour simulation. The black dots represent the center of the pollutant parcels. The size and height of each parcel are not depicted. In most cases, we compare the plume trajectories for the cases of prevailing wind direction equal to 180 and 360 degrees. Note: for accurate concentration computations a larger number of parcels must be released per unit time.

Seven hours after the start of the plume simulation (fig. 6), the pollutants have traveled over fifty kilometers to the east due to the westerly winds. The plume is very narrow, evidence of the lack of turbulent mixing present in night time stable environments. When the prevailing wind direction is 180 degrees, the plume travels slightly to the north and impacts on the coastal range mountain peak. When the prevailing wind direction is 360 degrees, the plume travels slightly to the south through the coastal range pass.

At 11:00 am, we see a very interesting feature: the plume is narrow between the source and about 281 km east-utm, and then to the east the plume suddenly expands in width (fig. 7). This most likely results from the elevated plume impinging upon the land-surface boundary layer (also known as a thermal internal boundary layer - TIBL), which is growing in height with time of day and distance from the coast.

By afternoon, evidence of the sea-breeze effect is apparent (fig. 8). For a prevailing wind direction of 180 degrees, the plume has spread out laterally and some of the pollution even extends over the ocean. When the prevailing wind is 360 degrees, a cloud of pollution travels slowly to the west, but very little reaches the ocean. In both cases, the near-stack plume travels to the west, indicating that the plume rise is large (recall from fig. 4 that the surface-level winds are from the west and the elevated winds are from the east).

By evening, the winds have become predominately onshore and the air pollution that was caught in the sea-breeze circulation is advected inland (fig. 9). When comparing the prevailing wind direction of 180 and 360 degrees, it is seen that the pollutant parcels are located to the north of the Ventanas site in the former case and to the south in the latter case.

Shifts in prevailing upper-level wind direction of 90 degrees has clearly had a large effect on the transport of the Ventanas air pollution (e.g., fig. 8). Although the mesoscale and microscale influence of the

ocean and mountains clearly dominates the flow structure, the relatively light, larger-scale driving winds typical of summer-time conditions alter the flow field enough to significantly impact plume transport. This result suggests further analysis of wind direction shifts of 30 to 60 degrees, which may represent the accuracy of synoptic-scale model-derived and rawinsonde-measured winds in relatively calm conditions. Further studies with stronger synoptic-scale winds and smaller wind direction shifts might also be warranted.

CONCLUSIONS

The sensitivity of plume dispersion to variations in the prescribed wind direction was tested in a coastal-mountain environment in Chile. Meteorological and plume dispersion simulations were performed with the HOTMAC mesoscale meteorological model and the RAPTAD Lagrangian dispersion model, respectively. These tests were motivated by our desire to develop a climatology of plume transport direction based on prevailing wind direction, as well as to evaluate the effect of the uncertainties inherent in rawinsonde wind measurements and large-scale weather wind-field forecasts, which are often used as input to meteorological models.

Model simulations were run with an upper-level wind speed of 1.6 m/s and with three different prevailing wind directions: 180, 270, and 360 degrees. We found that surface-level winds were not very sensitive to prevailing upper-level wind direction changes of 180 degrees. However, daytime winds at plume centerline height (approximately 400 m) were significantly affected by the prevailing wind direction. Comparison of plume transport for the cases of prevailing wind direction equal to 180 and 360 degrees revealed that local-scale flow patterns dominated the plume transport. For most of the night and part of the day, strong onshore flow advected the plume inland. However, for a southerly prevailing wind the plume was transported slightly to the north and for a northerly prevailing wind the plume was transported slightly to the south. Except for the case of prevailing wind direction equal to 270 degrees, we found that significant plume growth resulted from plume impingement on the developing boundary layer and plume entrapment in the sea-breeze circulation. After nearly a day of plume simulation, large differences were found in pollutant parcel location as a result of the different prevailing upper-level wind directions.

Acknowledgments. We wish to thank Mr. Rick Bradley and the US Department of Energy for their support of this project. The help of Luis Matamala of CIMM (Centro de Investigación Minería y Metalurgica) and Juan Scheib L., José Sanhueza R., and Alejandro Diez of ENAMI (La Empresa Nacional de Minería) was critical to the success of the project. In addition, Mr. Javier Vergara Fisher of the Comisión Especial de Descontaminación was also very helpful. At Los Alamos National Laboratory, Mr. Jorge Roman provided key assistance with topographical databases.

REFERENCES

1. C.M. Romo-Kroger, J.R. Morales, M.I. Dinator and F. Llona, “Heavy metals in the atmosphere coming from a copper smelter in Chile”, At. Env., 29(4): 705-711 (1994).
2. W.A. Lyons, R.A. Pielke, C.J. Tremback, R.L. Walko, D.A. Moon, and C.S. Keen, “Modeling impacts of mesoscale vertical motions upon coastal zone air pollution dispersion”, At. Env., 29(2): 283-301 (1995).
3. P.J. Hurley and P.C. Manins, “Meteorological modeling on high-ozone days in Perth, Western Australia”, J. Appl. Meteor., 34(7): 1643-1652 (1995).
4. R. Lu and R.P. Turco, “Air pollutant transport in a coastal environment. Part I. Two-dimensional simulations of sea-breeze and mountain effects”, J. At. Sci., 51(15): 2285-2308 (1994).
5. T. Yamada and S. Bunker, “Development of a nested grid, second moment turbulence closure model and application to the 1982 ASCOT Brush Creek data simulation”, J. Appl. Meteor., 27: 562-578 (1988).
6. G.I. Mellor and T. Yamada, “Development of a turbulence closure model for geophysical fluid prob-

lems", Rev.Geophys. Space Phys., 20(4): 851-875 (1982).
7. T. Yamada, "Simulations of nocturnal drainage flows by a q^2l turbulence closure model", J. Atm. Sci., 40(1): 91-106 (1983).
8. T. Yamada and S. Bunker, "A numerical model study of nocturnal drainage flows with strong wind and temperature gradients", J. Appl. Meteor., 28: 545-554 (1989).
9. M. Willliams, M. Brown, X. Cruz, G. Sosa, and G. Streit, "Development and testing of meteorology and air dispersion models for Mexico City", At. Env., 29(21): 2929-2960 (1995).
10. M. Willliams and T. Yamada, "A microcomputer-based forecasting model: potential applications for emergency response plans and air quality studies", J. Air Waste Manage. Assoc., 40: 1266-1274 (1990).
11. J.T. Lee and G. L. Stone, "The use of Eulerian initial conditions in a Lagrangian model of turbulent diffusion", Los Alamos National Laboratory, LA-UR-82-3034, Los Alamos, NM (1982).
12. G. Briggs, "Plume rise and buoyancy effects" in Atmospheric Science and Power Production (ed. D. Randerson), U.S. Dept. of Energy, DOE/TIC-27601, pp 327-366 (1984).

Table 1: Horizontal grid parameters

mesh type	SW corner (utm, km)	grid size (km)	no. of grids E-W dir.	no. of grids N-S dir.
coarse	209, 6189	18	10	14
medium	245, 6297	6	15	21
fine	263, 6351	2	12	18

Table 2: Vertical mesh coordinates

parameter	grid heights (m)
$\overline{U}$, $\overline{V}$, $\overline{\Theta}$, $\overline{Q}$	0 4 8 12 16 53 154 321 553 850 1212 1640 2132 2690 3312 4000
$\overline{W}$, q^2, K_m, K_h	0 2 6 10 14 26 95 230 429 693 1023 1418 1878 2403 2993 3648

Table 3: Stack parameters

parameter	stack #1	stack #2	combined stack
stack height (m)	155	155	155
stack diameter (m)	2	3	3.4
temperature (K)	530	545	537.9
vertical velocity (m/s)	6	3	4.4
source strength (g/s)	2395	1551	3946

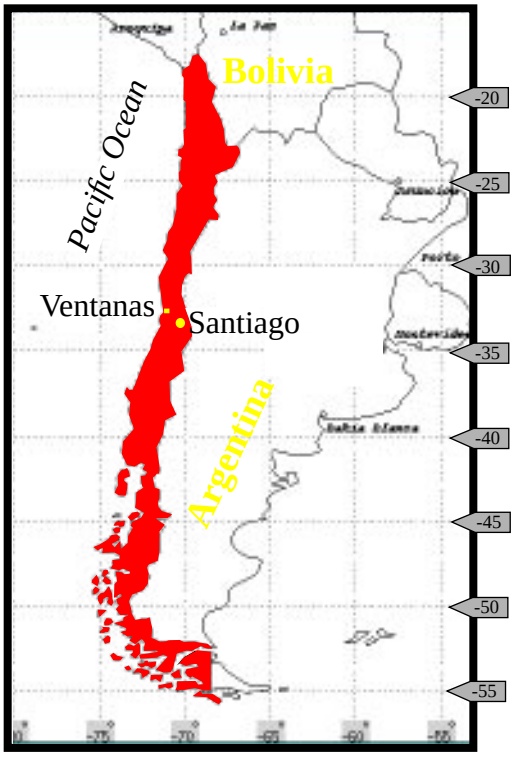

Figure 1. Map of Chile. The Ventanas smelter is approximately 100 km northwest of Santiago.

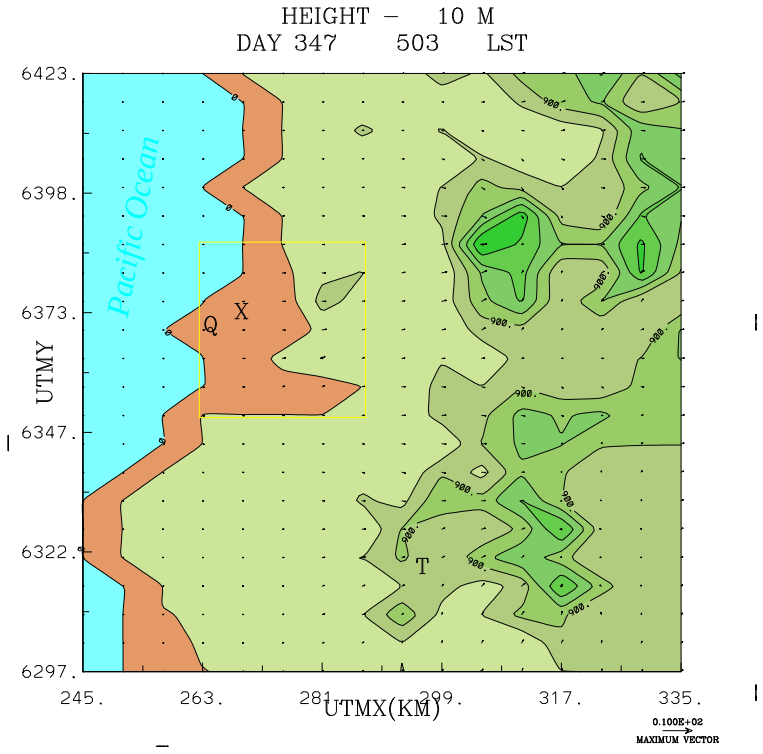

Figure 2. Typical night time horizontal winds computed by the HOTMAC model for prevailing upper-level wind direction equal to 270 degrees. Computed on the intermediate grid at a 10 m height. X and Q denote the locations of the Ventanas smelter and town of Quinteros, respectively. Santiago is located outside the intermediate grid at utm coordinates (340 km, 6290 km).

a)

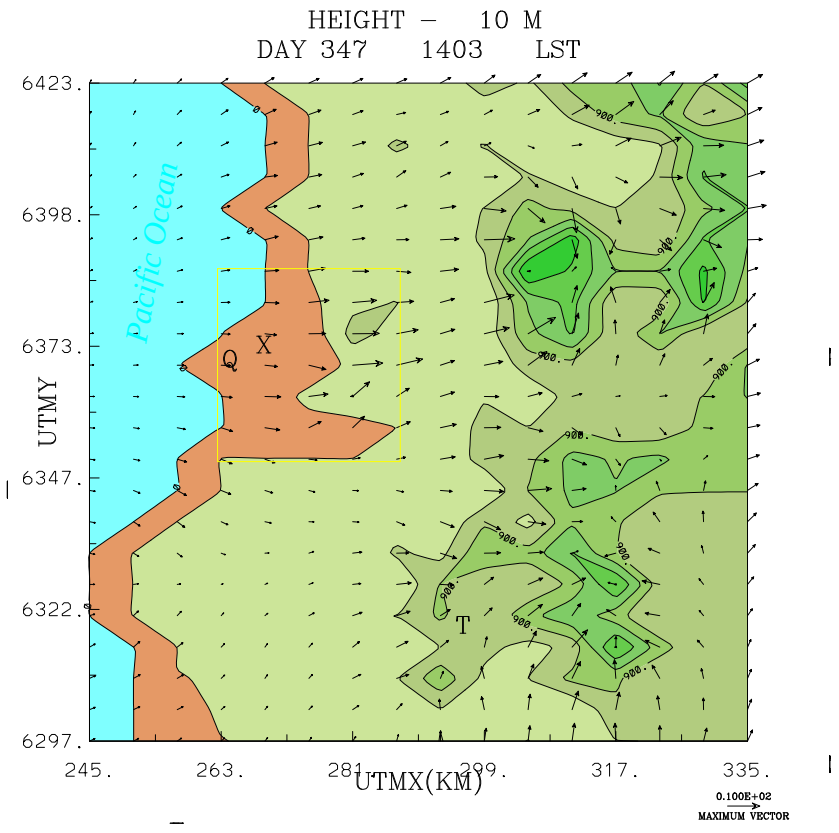

b)

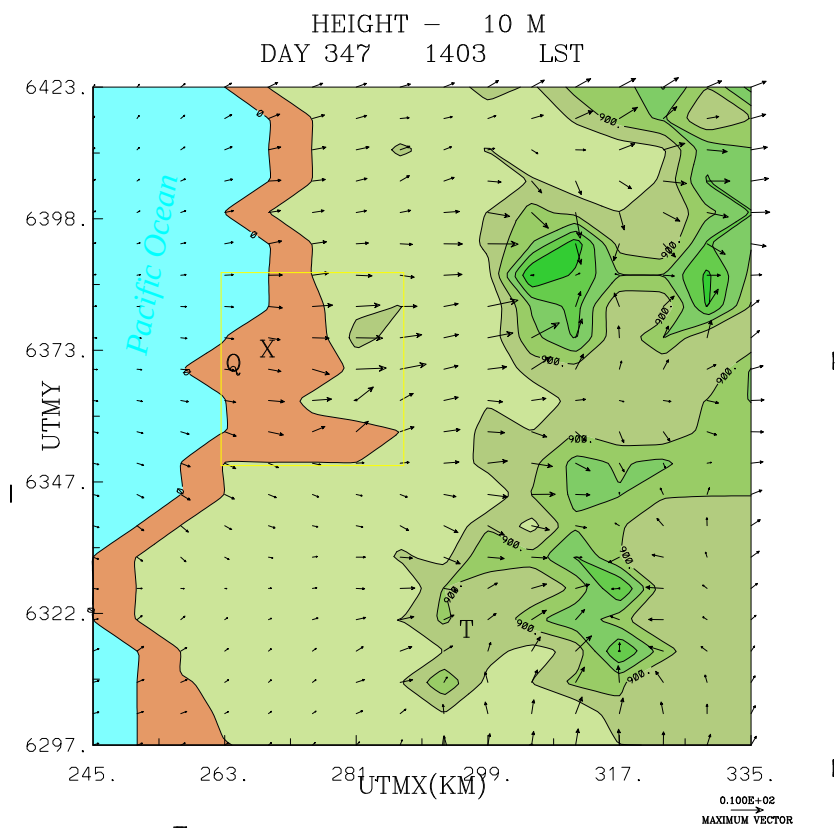

Figure 3. Typical daytime horizontal winds computed by the HOTMAC model for prevailing upper-level wind direction equal to a) 180 degrees and b) 360 degrees. Computed on the intermediate grid at a 10 m height. X and Q denote the locations of the Ventanas smelter and town of Quinteros, respectively.

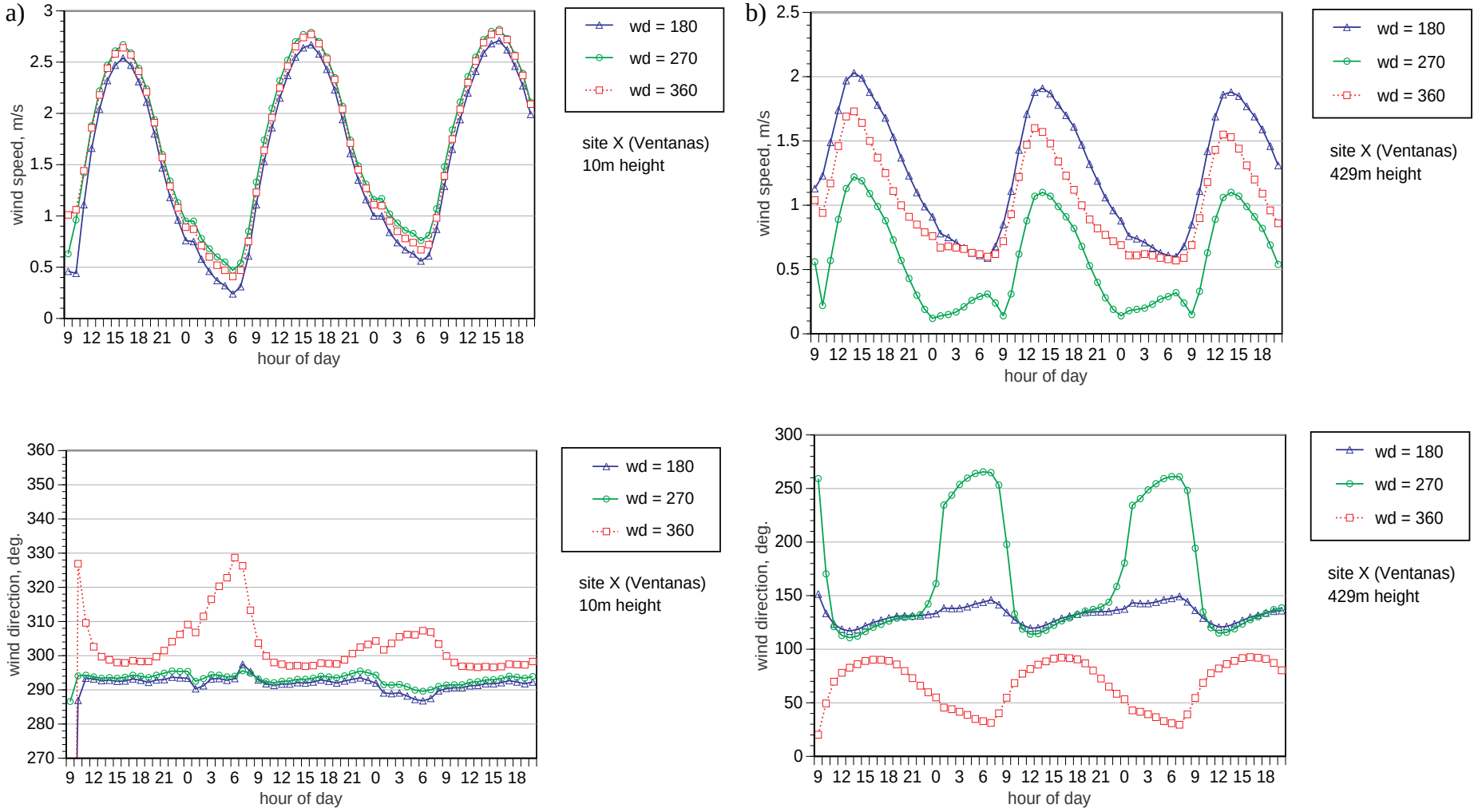

Figure 4. Model-computed wind speed and wind direction versus time for three different prevailing upper-level wind directions. Computations made at the Ventanas site at a height of a) 10 m and b) 429 m. The upper-level wind speed maximum is 1.6 m/s. Simulation start time: 8:00 am, Dec. 11.

a)

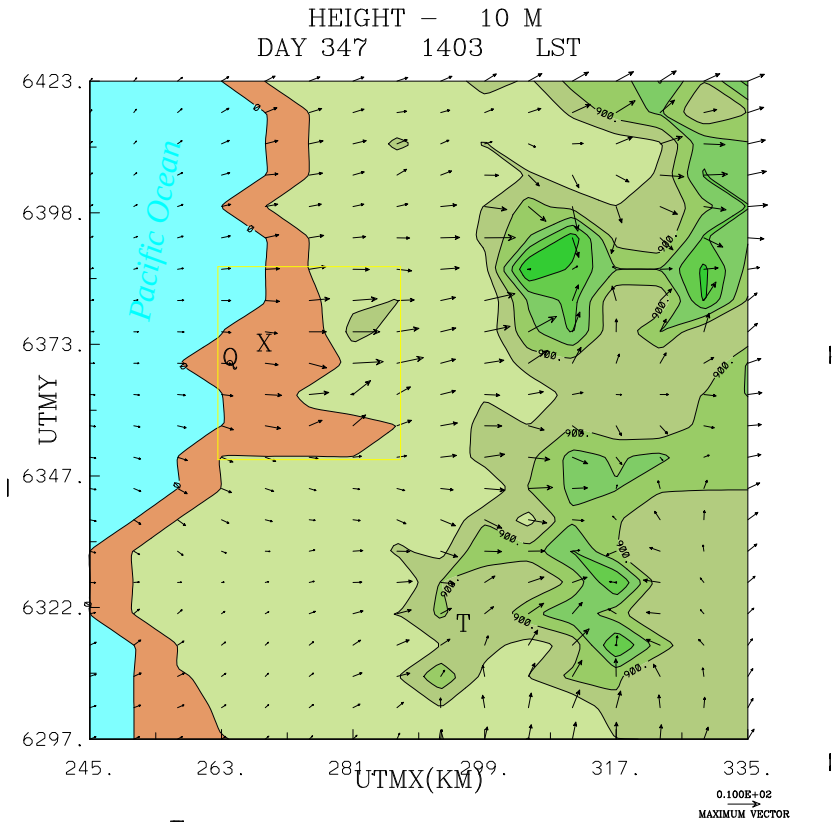

b)

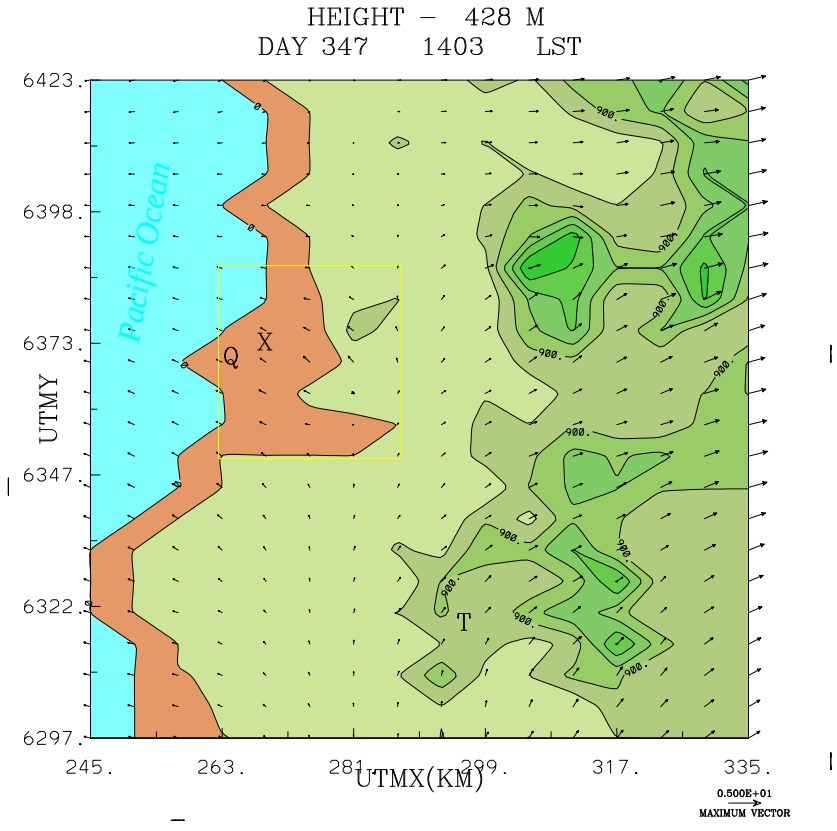

Figure 5. Typical afternoon horizontal winds computed by the HOTMAC model at a height of a) 10 m and b) 428 m show a sea-breeze circulation. Computed on the intermediate grid with a prevailing upper-level wind direction of 270 degrees. Note the change in the scale of the maximum wind vector.

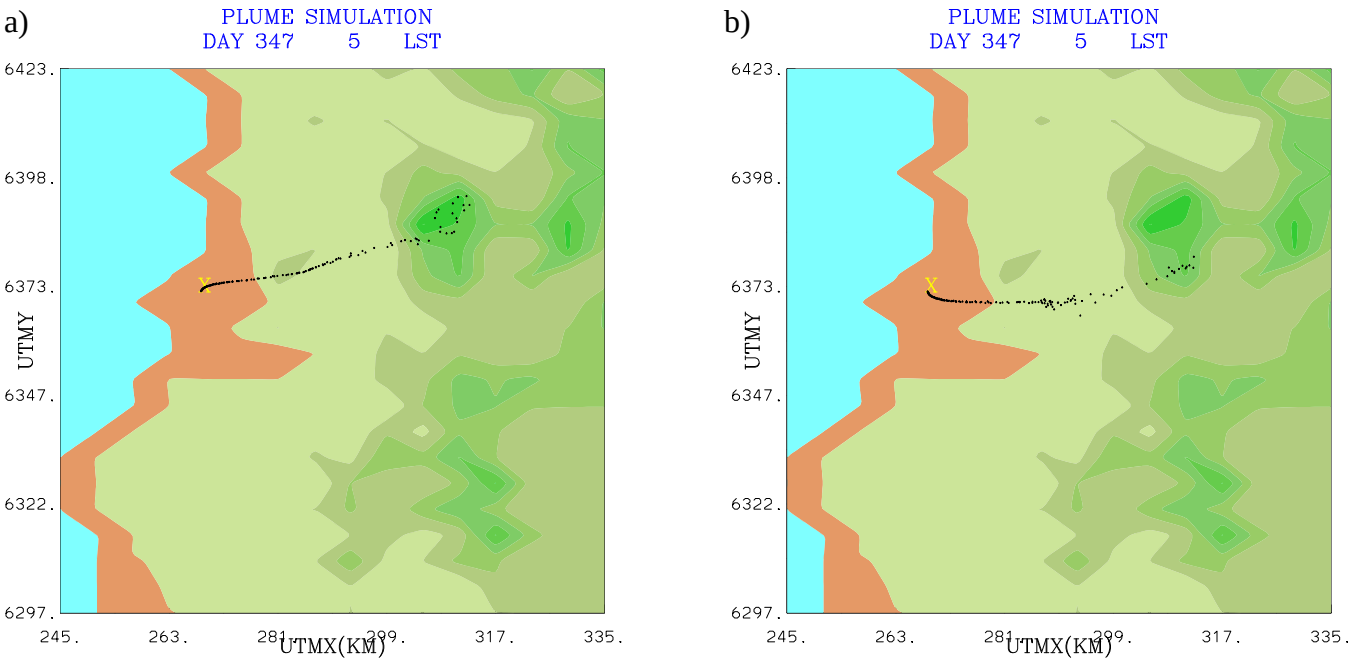

Figure 6. Simulation of the Ventanas plume during pre-dawn hours by the RAPTAD model for an upper-level prevailing wind direction equal to a) 180 and b) 360 degrees. Plume release start time at 9 pm on Dec. 11. Elapsed time: 8 hours.

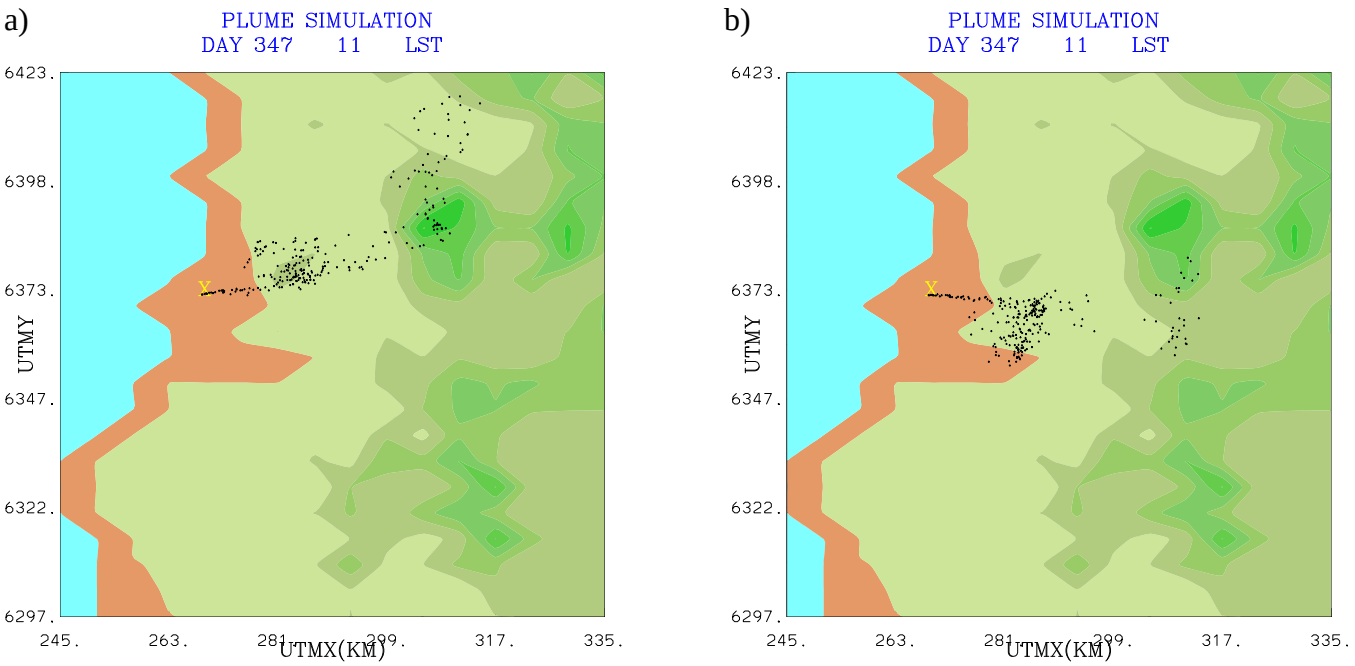

Figure 7. Simulation of the Ventanas plume during late morning hours by the RAPTAD model for upper-level prevailing wind direction equal to a) 180 and b) 360 degrees. Elapsed time: 14 hours.

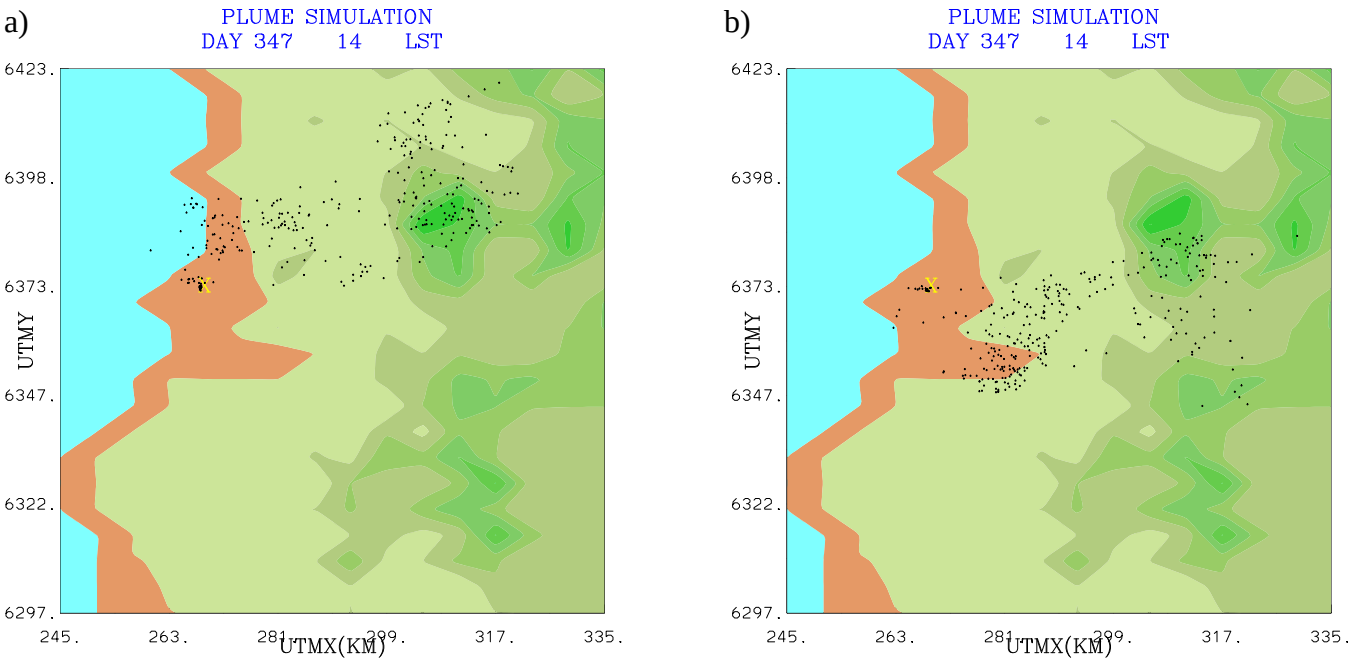

Figure 8. Simulation of the Ventanas plume during mid-afternoon hours by the RAPTAD model for upper-level prevailing wind direction equal to a) 180 and b) 360 degrees. Elapsed time: 17 hours.

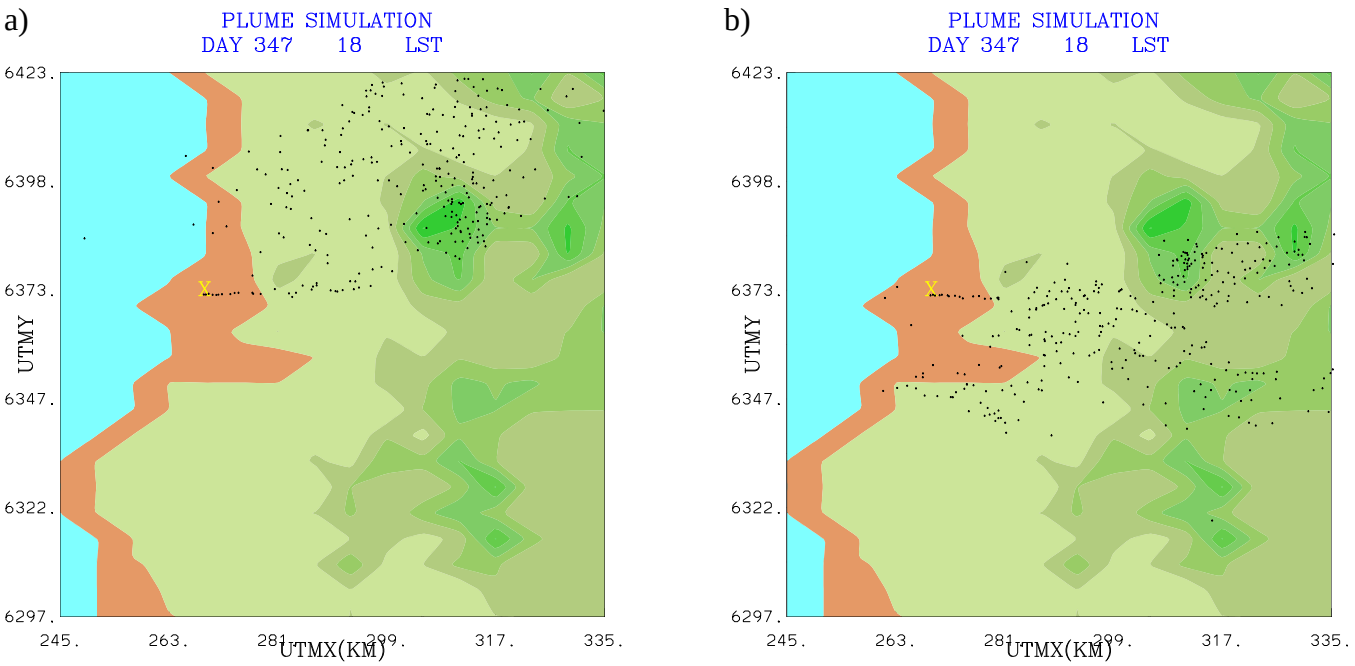

Figure 9. Simulation of the Ventanas plume during early-evening hours by the RAPTAD model for upper-level prevailing wind direction equal to a) 180 and b) 360 degrees. Elapsed time: 21 hours.